

Remote entanglement via adiabatic passage using a tunably-dissipative quantum communication system

H.-S. Chang,¹ Y. P. Zhong,¹ A. Bienfait,^{1,*} M.-H. Chou,^{1,2} C. R. Conner,¹ É. Dumur,^{1,3,†}
J. Grebel,¹ G. A. Peairs,^{4,1} R. G. Povey,^{1,2} K. J. Satzinger,^{4,1,‡} and A. N. Cleland^{1,3}

¹*Pritzker School of Molecular Engineering, University of Chicago, Chicago IL 60637, USA*

²*Department of Physics, University of Chicago, Chicago IL 60637, USA*

³*Argonne National Laboratory, Argonne IL 60439, USA*

⁴*Department of Physics, University of California, Santa Barbara CA 93106, USA*

(Dated: May 27, 2020)

Effective quantum communication between remote quantum nodes requires high fidelity quantum state transfer and remote entanglement generation. Recent experiments have demonstrated that microwave photons, as well as phonons, can be used to couple superconducting qubits, with a fidelity limited primarily by loss in the communication channel [1–6]. Adiabatic protocols can overcome channel loss by transferring quantum states without populating the lossy communication channel. Here we present a unique superconducting quantum communication system, comprising two superconducting qubits connected by a 0.73 m-long communication channel. Significantly, we can introduce large tunable loss to the channel, allowing exploration of different entanglement protocols in the presence of dissipation. When set for minimum loss in the channel, we demonstrate an adiabatic quantum state transfer protocol that achieves 99% transfer efficiency as well as the deterministic generation of entangled Bell states with a fidelity of 96%, all without populating the intervening communication channel, and competitive with a qubit-resonant mode-qubit relay method. We also explore the performance of the adiabatic protocol in the presence of significant channel loss, and show that the adiabatic protocol protects against loss in the channel, achieving higher state transfer and entanglement fidelities than the relay method.

* Present address: Université de Lyon, ENS de Lyon, Université Claude Bernard, CNRS, Laboratoire de Physique, F-69342 Lyon, France

† Present address: Université Grenoble Alpes, CEA, INAC-Pheliqs, 38000 Grenoble, France

‡ Present address: Google, Santa Barbara CA 93117, USA.

Remote entanglement of superconducting qubits has recently been demonstrated using both microwave photon- and phonon-mediated communication [1–6]. Many of these demonstrations are limited by loss in the communication channel, due to loss in the various microwave components or intrinsic to the channel itself [1, 4, 6]; similar limitations apply to e.g. optically-based quantum communication systems. Adiabatic protocols analogous to stimulated Raman adiabatic passage (STIRAP) [7, 8] can mitigate such loss by adiabatically evolving an eigenstate of the system, using states that are “dark” with respect to the communication channel. These enable the high-fidelity coherent transfer of quantum states between sender and receiver nodes, even in the presence of large channel loss. Despite their use in a number of localized systems, such protocols have not been used for the generation of remote entangled states [7, 8].

In this Letter, we present a unique experimental system comprising a pair of superconducting transmon-style qubits linked by an on-chip, 0.73 m-long superconducting microwave transmission line. By changing the coupling of the transmission line to a resistive load, we can vary the transmission line’s energy lifetime T_{1r} over two orders of magnitude. We demonstrate an adiabatic protocol for quantum communication between the qubit nodes, compare its performance to a qubit-transmission mode-qubit relay method [5, 9, 10], and explore the performance of both protocols as a function of transmission loss.

We first describe the experimental device, then the two state transfer methods. We test the performance of each protocol in the low-loss limit, then as a function of transmission loss. The adiabatic process achieves significantly improved performance compared to the relay method, especially at intermediate levels of loss in the channel.

The two quantum state transfer methods, and the device we use to test them, are shown in Fig. 1. The device comprises two frequency-tunable superconducting xmon qubits [11, 12], Q_1 and Q_2 , each coupled to one end of the on-chip transmission line via an electrically-controlled tunable coupler [13], G_1 and G_2 respectively (Fig. 1b). We use the qubit ground $|g\rangle$ and excited $|e\rangle$ states, whose transition frequency is tunable from ~ 3 to 6 GHz. Qubit control is via low-frequency flux-tuning for Z control and quadrature-resolved microwave pulses for XY control. We read out the qubit states using standard dispersive measurements [14–16], via a capacitively-coupled readout resonator and a traveling-wave parametric amplifier. We projectively measure the excited state probability P_e of each qubit with a fidelity of $88.8 \pm 0.8\%$.

The tunable couplers G_1 and G_2 allow us to externally control the coupling $g_{1,2}$ of each qubit to the individual resonant modes in the transmission line. A variable control consisting of two additional tunable couplers, D_1 and D_2 , is integrated into the transmission line, 1.6 mm from the coupler G_1 and its associated qubit Q_1 . This circuit element provides electrically-controlled coupling between its input port and two output ports [17]. The coupler D_2 is placed inline with the transmission line and is always set to provide maximum coupling (and minimal reflection) to the remaining length of transmission line. The other coupler D_1 connects to port 1 on the sample mount, which is terminated by a lumped 50Ω microwave load outside the sample box. Varying the coupling to this load allows us to set the loss in the transmission line, quantified by the energy lifetime T_{1r} of each resonant mode.

The transmission line of length $\ell = 0.73$ m supports multiple resonant modes, separated in frequency by the free spectral range $\omega_{\text{FSR}}/2\pi = 1/2T_\ell = 84$ MHz, where $T_\ell = 5.9$ ns is the photon one-way transit time in the channel. For sufficiently small qubit-resonator coupling, $g_{1,2} \ll \omega_{\text{FSR}}$, each qubit can be selectively coupled to a single resonant mode in the transmission line. This is shown in Fig. 2a, where the transition frequency $\omega_{ge}/2\pi$ of qubit Q_1 is tuned over 400 MHz, yielding four separate vacuum Rabi swap resonances spaced by the free spectral range $\omega_{\text{FSR}}/2\pi$. The loss coupler D_1 was set to minimum coupling, so the transmission line is limited only by its intrinsic loss. All experiments here were done with the mode at 5.351 GHz, just to the right of center in Fig. 2a.

In Fig. 2b, we demonstrate tunable control over the channel loss, using qubit Q_1 to measure the lifetime of the resonant mode

at 5.531 GHz as we vary the coupler D_1 and thus the transmission line loss. The pulse sequence for this measurement is shown inset in Fig. 2b. The mode energy decay time T_{1r} for each loss setting (controlled by the D_1 flux) is shown in Fig. 2b. With no coupling through D_1 , we measure the intrinsic resonant mode lifetime $T_{1r} \approx 3410 \pm 40$ ns (orange), comparable to similar transmission lines without variable loss [5]. With maximum coupling to the load, we measure a lifetime $T_{1r} \approx 28.7 \pm 0.2$ ns (blue), corresponding to a loaded quality factor $Q_r = 960$, about 120 times smaller than the intrinsic quality factor of 1.1×10^5 . We also measure the resonant mode's Ramsey dephasing time T_{2r} at various D_1 flux bias points, and find $T_{2r} \approx 2T_{1r}$, indicating the coupler D_1 introduces negligible additional phase decoherence. One non-ideality with this system is that qubit Q_1 , due to its close proximity to the loss coupler D_1 , also has its lifetime reduced when the couplers G_1 and D_1 are both set to non-zero coupling, allowing energy loss from Q_1 to the external load; this limits Q_1 's performance, and is discussed further in the Supplementary Information [18]. We note that this non-ideality can be avoided by placing the loss coupler D_1 in the middle of transmission line, as the transmission line would protect both qubits from the external load.

We used two different communication protocols, adiabatic transfer and a qubit-resonant mode-qubit relay method. Both methods were used for qubit state transfer via the transmission line as well as Bell state generation, both as a function of loss in the communication channel. The relay method uses a single extended mode in the transmission line, swapping an excitation from one qubit into that mode and subsequently swapping the excitation from that mode to the other qubit. This method is described in detail elsewhere [5]; here it achieves an intrinsic loss-limited state transfer efficiency of $\eta = 0.95 \pm 0.01$ and a Bell state fidelity of $\mathcal{F}_s = \langle \psi^- | \rho | \psi^- \rangle = 0.941 \pm 0.005$, where ρ is the measured density matrix and $|\psi^-\rangle = (|eg\rangle - |ge\rangle) / \sqrt{2}$ is the reference Bell singlet state.

The adiabatic method uses the variable coupling of each qubit to the transmission line. When qubits Q_1 and Q_2 are set to the same frequency and couple to the same resonant mode in the channel with strengths $g_1(t)$ and $g_2(t)$, the single-excitation Hamiltonian for the system can be written in the rotating frame as

$$H/\hbar = g_1(t) (|e0g\rangle\langle g1g| + |g1g\rangle\langle e0g|) + g_2(t) (|g0e\rangle\langle g1g| + |g1g\rangle\langle g0e|), \quad (1)$$

where $|aNb\rangle$ corresponds to Q_1 (Q_2) in $|a\rangle$ ($|b\rangle$) with N photons in the resonant transmission line mode. This Hamiltonian supports a ‘‘dark’’ eigenstate $|D\rangle$ that has no occupancy in the resonant mode,

$$|D(t)\rangle = \frac{1}{\sqrt{2}} (\cos \theta(t) |e0g\rangle - \sin \theta(t) |g0e\rangle), \quad (2)$$

where the mixing angle θ is given by $\tan \theta(t) = g_1(t)/g_2(t)$. With g_1 set to zero and g_2 to its maximum, the dark state is $|D\rangle = |e0g\rangle$, while exchanging the coupling values $g_1 \leftrightarrow g_2$ yields the dark state $|g0e\rangle$. By adiabatically varying the ratio $g_1(t)/g_2(t)$ in time from zero to its maximum, the system will swap the excitation from Q_1 to Q_2 , without populating the lossy intermediate channel [7, 19].

Here, we implement a simple adiabatic scheme [19, 20], where we vary the couplings in time according to $g_1(t) = \bar{g} \sin(\pi t/2t_f)$ and $g_2(t) = \bar{g} \cos(\pi t/2t_f)$. We choose the parameters $\bar{g}/2\pi = 15$ MHz and $t_f = 132$ ns, minimizing the impact of finite qubit coherence while maintaining sufficient adiabaticity (see [18]). We note that the adiabatic protocol supports better than 90% transfer efficiency even when $\bar{g} = 0.4 \omega_{\text{FSR}}$; see [18].

In Fig. 3a, we demonstrate deterministic adiabatic state transfer from Q_1 to Q_2 . With Q_1 in $|e\rangle$ and Q_1 and Q_2 set on-resonance with a single mode in the channel, we adjust the couplers G_1 and G_2 adiabatically to complete the state transfer. We show the excited state population of each qubit as a function of time t , measured with the resonant mode loss at its intrinsic minimum. We observe the expected gradual population transfer from Q_1 to Q_2 , with Q_2 's population reaching its maximum at

$t = t_f$, with a transfer efficiency $\eta = P_{e,Q_2}(t = t_f)/P_{e,Q_1}(t = 0) = 0.99 \pm 0.01$. We further characterize the state transfer by carrying out quantum process tomography [21], yielding the process matrix χ shown inset in Fig. 3a, with a process fidelity $\mathcal{F}_p = 0.96 \pm 0.01$, limited by qubit decoherence. The process matrix calculated from a master equation simulation displays a small trace distance to the measured χ matrix of $\mathcal{D} = \sqrt{\text{Tr}([\chi - \chi_{\text{sim}}]^2)} = 0.02 \pm 0.01$, indicating excellent agreement with experiment.

The adiabatic protocol can also be used to generate remote entanglement between Q_1 and Q_2 . With Q_1 prepared in $|e\rangle$, we share half its excitation with Q_2 using the adiabatic protocol, by stopping the transfer at its midpoint $t = t_f/2$. This generates a Bell singlet state $|\psi^-\rangle = (|eg\rangle - |ge\rangle)/\sqrt{2}$. The qubit excited state population is shown as function of time t in Fig. 3b. We further characterize the Bell state by quantum state tomography [22, 23], and the reconstructed density matrix ρ is shown inset in Fig. 3b. We find a Bell state fidelity $\mathcal{F}_s = \langle \psi^- | \rho | \psi^- \rangle = 0.964 \pm 0.007$, referenced to the ideal Bell singlet state ψ^- , and a concurrence $\mathcal{C} = 0.95 \pm 0.01$ (see [18]). The density matrix ρ_{sim} calculated from a master equation simulation shows a small trace distance to the measured ρ , $\sqrt{\text{Tr}(|\rho - \rho_{\text{sim}}|^2)} = 0.01$, indicating excellent agreement with experiment.

We explore the impact of loss on both the relay method and the adiabatic protocol, with results shown as a function of the resonant channel mode energy lifetime T_{1r} in Fig 4. For the highest level of dissipation, with $T_{1r} = 28.7$ ns, we measure an adiabatic transfer efficiency $\eta = 0.67 \pm 0.01$, even though the transfer time t_f is four times the resonant mode lifetime. The efficiency is primarily limited by loss in qubit Q_1 due to its spurious coupling loss through D_1 to the 50Ω load (see [18]), in good agreement with master equation simulations. Results from a simulation without the spurious coupling are plotted as black dashed lines in Fig 4a, limited by a small channel occupation due to the finite adiabaticity of the sequence. We compare these results to the relay method, where we use a weak coupling $|g_{1,2}|/2\pi = 5.0$ MHz to ensure the qubits only couple to a single transmission line mode; this results in a total transfer time $2\tau_{\text{swap}} = 100$ ns. We find the adiabatic protocol consistently performs better than the relay method, with a $2.6\times$ higher transfer efficiency η ($2.3\times$ reduction in transfer loss) and $1.5\times$ higher process fidelity \mathcal{F}_p ($2.3\times$ reduction in process infidelity) compared to the relay method in the most dissipative case; the adiabatic protocol is primarily limited by spurious coupling loss in Q_1 , while the relay method is limited by loss in the channel (see [18]).

In Fig. 4b, we display the entanglement fidelity using the adiabatic protocol with different levels of channel loss, and compare to the relay method. The adiabatic protocol outperforms the relay method in all levels of dissipation. At the highest loss level, where $T_{1r} = 28.7$ ns, the adiabatic protocol achieves $1.2\times$ higher Bell state fidelity \mathcal{F}_s ($1.5\times$ reduction in Bell state infidelity) and $1.3\times$ higher concurrence \mathcal{C} ($1.7\times$ reduction in concurrence infidelity) compared to the relay method; the spurious-coupling-free simulation result for the adiabatic protocol is shown by the black dashed lines, limited by a small channel occupation due to the finite adiabaticity of the sequence.

In conclusion, we describe a unique experimental system in which we can explore the performance of quantum communication protocols in the presence of controllable communication loss. We demonstrate an adiabatic protocol that realizes high-fidelity transfer of quantum states and entangled Bell states, limited mostly by spurious coupling of one qubit to the controlled transmission line loss. The platform we have developed is well-suited to explore the impact of channel loss on other error-protecting quantum communication protocols, such as heralding [24–26] and entanglement distillation [27–29]. The ability to introduce controlled loss dynamically into the system opens the door to study dissipative dynamics in non-equilibrium systems, enabling approaches such as reservoir engineering [30, 31]. The adiabatic protocol demonstrated here is applicable to other quantum communication systems, for example phonon-based systems where the communication channel is significantly more lossy [6, 32, 33]. Future demonstrations could employ more advanced adiabatic protocols such as shortcuts to adiabaticity [34, 35] and composite adiabatic passage [36, 37] to further improve fidelity.

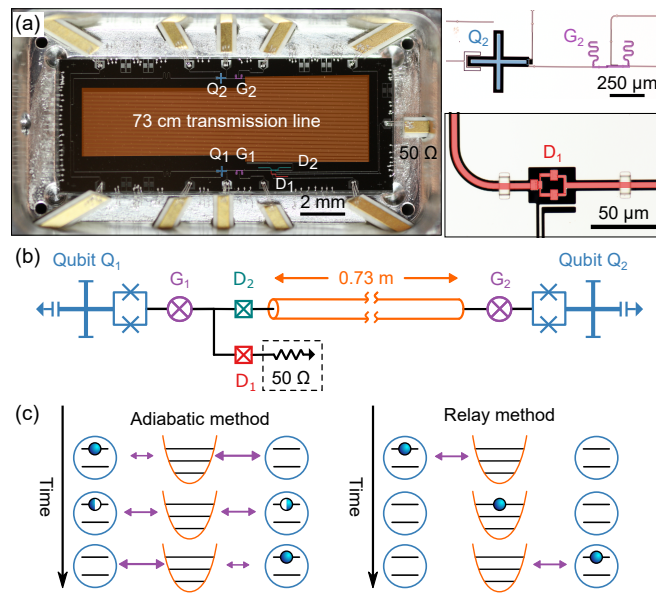


Figure 1. Experimental device. (a) Optical micrograph of the device (left), with magnified views of one qubit and its associated tunable coupler (right top), and one variable loss coupler (right bottom). (b) A simplified circuit schematic, with two superconducting qubits (Q_1 and Q_2 , blue), coupled by tunable couplers (G_1 and G_2 , purple) to a 0.73 m-long superconducting transmission line (orange). The transmission line is interrupted near Q_1 by a tunable switch. The switch comprises two tunable couplers D_1 (red) and D_2 (teal), with D_1 connected to an external 50Ω load to ground (dashed box), while D_2 connects to the remainder of the transmission line. Complete circuit diagram and parameters are provided in [18].

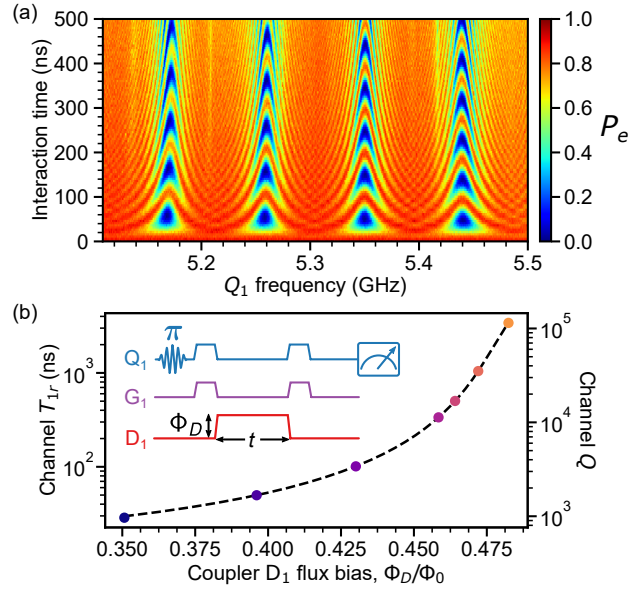


Figure 2. Variable loss transmission channel. (a) Vacuum Rabi swaps between qubit Q_1 and four sequential resonant transmission line modes. The coupling is set to $|g_1|/2\pi = 5.0 \pm 0.1$ MHz $\ll \omega_{\text{FSR}}/2\pi$. (b) Measurement of the energy lifetime T_{1r} of one resonant mode in the transmission line, at 5.351 GHz, with equivalent quality factors Q shown on right; inset shows pulse sequence. A π pulse to qubit Q_1 puts it in the excited state, and this excitation is swapped into the resonant mode for a time t , after which it is recovered and the qubit P_e measured. The corresponding lifetime is measured as a function of transmission line loss, controlled during the lifetime measurement using coupler D_1 . With D_1 turned off, we find the intrinsic lifetime $T_{1r} = 3410 \pm 40$ ns (orange); with maximum loss, we find $T_{1r} = 28.7 \pm 0.2$ ns (blue). The standard deviation of each data point is smaller than the points. Dashed lines are results calculated with a circuit model; see [18].

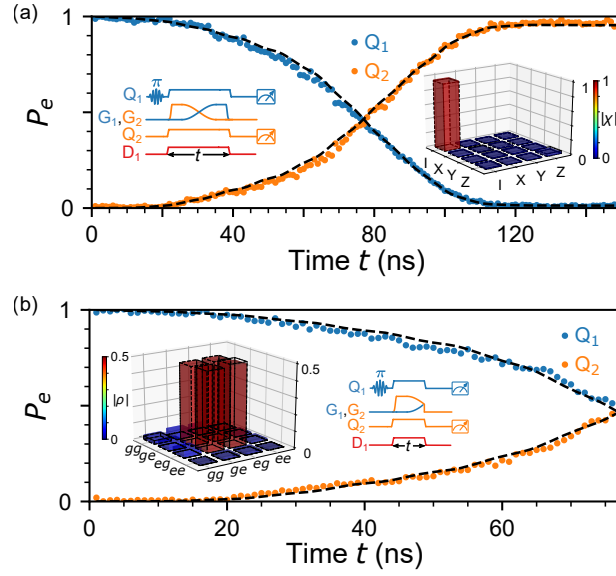


Figure 3. Quantum state transfer and remote entanglement using the adiabatic protocol. (a) Adiabatic state transfer between qubits Q_1 and Q_2 , measured with intrinsic loss in the transmission line. Blue (orange) circles represent excited state populations of Q_1 (Q_2) measured simultaneously at time t . Left inset: Control pulse sequence. The couplers are set so that coupling g_2 starts at its maximum with g_1 set to zero. Dissipation in the resonant channel mode is controlled using D_1 , here set to zero coupling. Right inset: Quantum process tomography, yielding a process fidelity $\mathcal{F}_p = 0.96 \pm 0.01$. (b) Adiabatic remote entanglement. Right inset shows control pulse sequence: With Q_1 initially prepared in $|e\rangle$, G_1 and G_2 are controlled using the adiabatic protocol to share half of Q_1 's excitation with Q_2 , resulting in a Bell singlet state $|\psi^-\rangle = (|eg\rangle - |ge\rangle)/\sqrt{2}$. Blue (orange) circles represent excited state populations of Q_1 (Q_2) measured simultaneously at time t . Left inset: Reconstructed density matrix of the final Bell state, yielding a state fidelity $\mathcal{F}_s = 0.964 \pm 0.007$ and concurrence $\mathcal{C} = 0.95 \pm 0.01$. In all panels, dashed lines are from master equation simulations accounting for channel dissipation and qubit imperfections (see [18]).

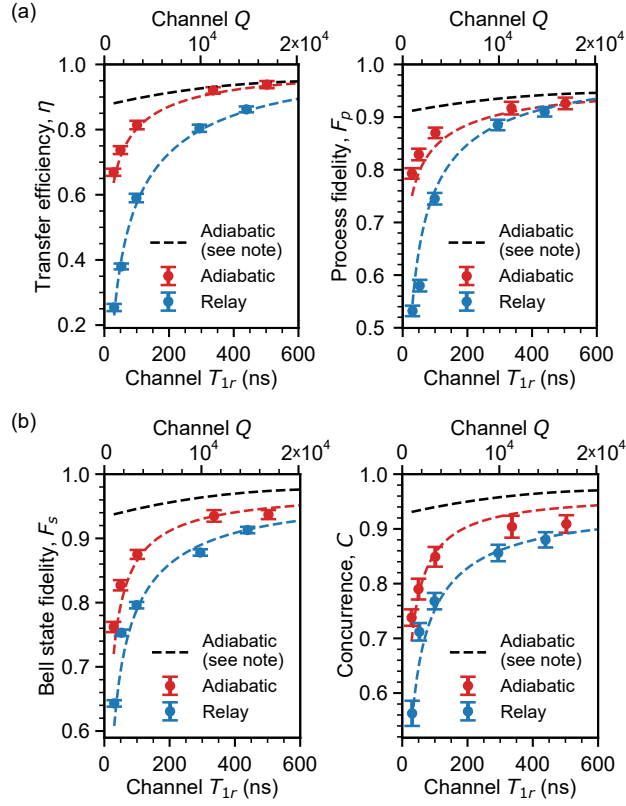


Figure 4. Quantum communication in the presence of channel loss, using both the relay method and adiabatic protocol. (a) Measured transfer efficiency η (left) and process fidelity \mathcal{F}_p (right) for the adiabatic protocol (red) and the relay method (blue), for different resonant channel mode lifetimes T_{1r} , with equivalent quality factors Q shown on top. (b) Measured Bell state fidelity \mathcal{F}_s (left) and concurrence \mathcal{C} (right) for adiabatic protocol (red) and relay method (blue). In all panels, error bars are one standard deviation; red and blue dashed lines are from simulations including all sources of loss and black dashed lines are from a master equation simulation for the adiabatic protocol with no Q_1 spurious coupling loss (see [18]).

ACKNOWLEDGMENTS

The authors thank A. A. Clerk, P. J. Duda, and B. B. Zhou for helpful discussions. We thank W. D. Oliver and G. Calusine at MIT Lincoln Lab for providing the traveling-wave parametric amplifier (TWPA) used in this work. Devices and experiments were supported by the Air Force Office of Scientific Research and the Army Research Laboratory. K.J.S. was supported by NSF GRFP (NSF DGE-1144085), É.D. was supported by LDRD funds from Argonne National Laboratory; A.N.C. was supported in part by the DOE, Office of Basic Energy Sciences. This work was partially supported by the UChicago MRSEC (NSF DMR-1420709) and made use of the Pritzker Nanofabrication Facility, which receives support from SHyNE, a node of the National Science Foundation's National Nanotechnology Coordinated Infrastructure (NSF NNCI-1542205). The authors declare no competing financial interests. Correspondence and requests for materials should be addressed to A. N. Cleland (anc@uchicago.edu).

-
- [1] P. Kurpiers, P. Magnard, T. Walter, B. Royer, M. Pechal, J. Heinsoo, Y. Salathe, A. Akin, S. Storz, J.-C. Besse, S. Gasparinetti, A. Blais, and A. Wallraff, *Nature* **558**, 264 (2018).
- [2] C. J. Axline, L. D. Burkhardt, W. Pfaff, M. Zhang, K. Chou, P. Campagne-Ibarcq, P. Reinhold, L. Frunzio, S. M. Girvin, L. Jiang, M. H. Devoret, and R. J. Schoelkopf, *Nature Physics* **14**, 705 (2018).
- [3] P. Campagne-Ibarcq, E. Zalys-Geller, A. Narla, S. Shankar, P. Reinhold, L. Burkhardt, C. Axline, W. Pfaff, L. Frunzio, R. J. Schoelkopf, and M. H. Devoret, *Physical Review Letters* **120**, 200501 (2018).
- [4] N. Leung, Y. Lu, S. Chakram, R. K. Naik, N. Earnest, R. Ma, K. Jacobs, A. N. Cleland, and D. I. Schuster, *npj Quantum Information* **5**, 18 (2019).
- [5] Y. P. Zhong, H.-S. Chang, K. J. Satzinger, M.-H. Chou, A. Bienfait, C. R. Conner, É. Dumur, J. Grebel, G. A. Peairs, R. G. Povey, D. I. Schuster, and A. N. Cleland, *Nature Physics* **15**, 741 (2019).
- [6] A. Bienfait, K. J. Satzinger, Y. P. Zhong, H.-S. Chang, M.-H. Chou, C. R. Conner, É. Dumur, J. Grebel, G. A. Peairs, R. G. Povey, and A. N. Cleland, *Science* **364**, 368 (2019).
- [7] N. V. Vitanov, A. A. Rangelov, B. W. Shore, and K. Bergmann, *Reviews of Modern Physics* **89**, 015006 (2017).
- [8] K. Bergmann, H.-C. Nagerl, C. Panda, G. Gabrielse, E. Miloglyadov, M. Quack, G. Seyfang, G. Wichmann, S. Ospelkaus, A. Kuhn, S. Longhi, A. Szameit, P. Pirro, B. Hillebrands, X.-F. Zhu, J. Zhu, M. Drewsen, W. K. Hensinger, S. Weidt, T. Halfmann, H.-L. Wang, G. S. Paraoanu, N. V. Vitanov, J. Mompart, T. Busch, T. J. Barnum, D. D. Grimes, R. W. Field, M. G. Raizen, E. Narevicius, M. Auzinsh, D. Budker, A. Plffy, and C. H. Keitel, *Journal of Physics B: Atomic, Molecular and Optical Physics* **52**, 202001 (2019).
- [9] M. A. Sillanpaa, J. I. Park, and R. W. Simmonds, *Nature* **449**, 438 (2007).
- [10] M. Ansmann, H. Wang, R. C. Bialczak, M. Hofheinz, E. Lucero, M. Neeley, A. D. O'Connell, D. Sank, M. Weides, J. Wenner, A. N. Cleland, and J. M. Martinis, *Nature* **461**, 504 (2009).
- [11] J. Koch, T. M. Yu, J. Gambetta, A. A. Houck, D. I. Schuster, J. Majer, A. Blais, M. H. Devoret, S. M. Girvin, and R. J. Schoelkopf, *Physical Review A* **76**, 042319 (2007).
- [12] R. Barends, J. Kelly, A. Megrant, D. Sank, E. Jeffrey, Y. Chen, Y. Yin, B. Chiaro, J. Mutus, C. Neill, P. O'Malley, P. Roushan, J. Wenner, T. C. White, A. N. Cleland, and J. M. Martinis, *Physical Review Letters* **111**, 080502 (2013).
- [13] Y. Chen, C. Neill, P. Roushan, N. Leung, M. Fang, R. Barends, J. Kelly, B. Campbell, Z. Chen, B. Chiaro, A. Dunsworth, E. Jeffrey, A. Megrant, J. Y. Mutus, P. J. J. O'Malley, C. M. Quintana, D. Sank, A. Vainsencher, J. Wenner, T. C. White, M. R. Geller, A. N. Cleland, and J. M. Martinis, *Physical Review Letters* **113**, 220502 (2014).
- [14] D. I. Schuster, A. Wallraff, A. Blais, L. Frunzio, R.-S. Huang, J. Majer, S. M. Girvin, and R. J. Schoelkopf, *Physical Review Letters* **94**, 123602 (2005).

- [15] A. Wallraff, D. I. Schuster, A. Blais, L. Frunzio, J. Majer, M. H. Devoret, S. M. Girvin, and R. J. Schoelkopf, *Physical Review Letters* **95**, 060501 (2005).
- [16] A. Blais, R.-S. Huang, A. Wallraff, S. M. Girvin, and R. J. Schoelkopf, *Physical Review A* **69**, 062320 (2004).
- [17] H.-S. Chang, Y. P. Zhong, K. J. Satzinger, M.-H. Chou, A. Bienfait, C. R. Conner, É. Dumur, J. Grebel, G. A. Peairs, R. G. Povey, and A. N. Cleland, In preparation (2020).
- [18] S. Material, .
- [19] Y.-D. Wang and A. A. Clerk, *New Journal of Physics* **14**, 105010 (2012).
- [20] Y.-D. Wang, R. Zhang, X.-B. Yan, and S. Chesi, *New Journal of Physics* **19**, 093016 (2017).
- [21] M. Neeley, M. Ansmann, R. C. Bialczak, M. Hofheinz, N. Katz, E. Lucero, A. O'Connell, H. Wang, A. N. Cleland, and J. M. Martinis, *Nature Physics* **4**, 523 (2008).
- [22] M. Steffen, M. Ansmann, R. C. Bialczak, N. Katz, E. Lucero, R. McDermott, M. Neeley, E. M. Weig, A. N. Cleland, and J. M. Martinis, *Science* **313**, 1423 (2006).
- [23] M. Neeley, R. C. Bialczak, M. Lenander, E. Lucero, M. Mariani, A. D. O'Connell, D. Sank, H. Wang, M. Weides, J. Wenner, Y. Yin, T. Yamamoto, A. N. Cleland, and J. M. Martinis, *Nature* **467**, 570 (2010).
- [24] P. J. Mosley, J. S. Lundeen, B. J. Smith, P. Wasylczyk, A. B. U'Ren, C. Silberhorn, and I. A. Walmsley, *Physical Review Letters* **100**, 133601 (2008).
- [25] K. Azuma, K. Tamaki, and H.-K. Lo, *Nature Communications* **6**, 6787 (2015).
- [26] P. Kurpiers, M. Pechal, B. Royer, P. Magnard, T. Walter, J. Heinsoo, Y. Salathe, A. Akin, S. Storz, J.-C. Besse, S. Gasparinetti, A. Blais, and A. Wallraff, *Physical Review Applied* **12**, 044067 (2019).
- [27] P. G. Kwiat, S. Barraza-Lopez, A. Stefanov, and N. Gisin, *Nature* **409**, 1014 (2001).
- [28] R. Dong, M. Lassen, J. Heersink, C. Marquardt, R. Filip, G. Leuchs, and U. L. Andersen, *Nature Physics* **4**, 919 (2008).
- [29] H. Takahashi, J. S. Neergaard-Nielsen, M. Takeuchi, M. Takeoka, K. Hayasaka, A. Furusawa, and M. Sasaki, *Nature Photonics* **4**, 178 (2010).
- [30] J. F. Poyatos, J. I. Cirac, and P. Zoller, *Physical Review Letters* **77**, 4728 (1996).
- [31] M. B. Plenio and S. F. Huelga, *Physical Review Letters* **88**, 197901 (2002).
- [32] S. Hermelin, S. Takada, M. Yamamoto, S. Tarucha, A. D. Wieck, L. Saminadayar, C. Bauerle, and T. Meunier, *Nature* **477**, 435 (2011).
- [33] R. P. G. McNeil, M. Kataoka, C. J. B. Ford, C. H. W. Barnes, D. Anderson, G. A. C. Jones, I. Farrer, and D. A. Ritchie, *Nature* **477**, 439 (2011).
- [34] A. Baksic, H. Ribeiro, and A. A. Clerk, *Physical Review Letters* **116**, 230503 (2016).
- [35] B. B. Zhou, A. Baksic, H. Ribeiro, C. G. Yale, F. J. Heremans, P. C. Jerger, A. Auer, G. Burkard, A. A. Clerk, and D. D. Awschalom, *Nature Physics* **13**, 330 (2017).
- [36] B. T. Torosov, S. Guerin, and N. V. Vitanov, *Physical Review Letters* **106**, 233001 (2011).
- [37] A. Bruns, G. T. Genov, M. Hain, N. V. Vitanov, and T. Halfmann, *Physical Review A* **98**, 053413 (2018).

Supplementary Materials for Remote entanglement via adiabatic passage using a tunably-dissipative quantum communication system

I. DEVICE AND EXPERIMENTAL SETUP

The experiment is carried out inside a dilution refrigerator with a base temperature below 10 mK. A detailed description of the experimental setup, as well as the process flow for the device fabrication, are provided in ref. 1. A circuit diagram is shown in Fig. S1 with detailed device parameters provided in Table S2.

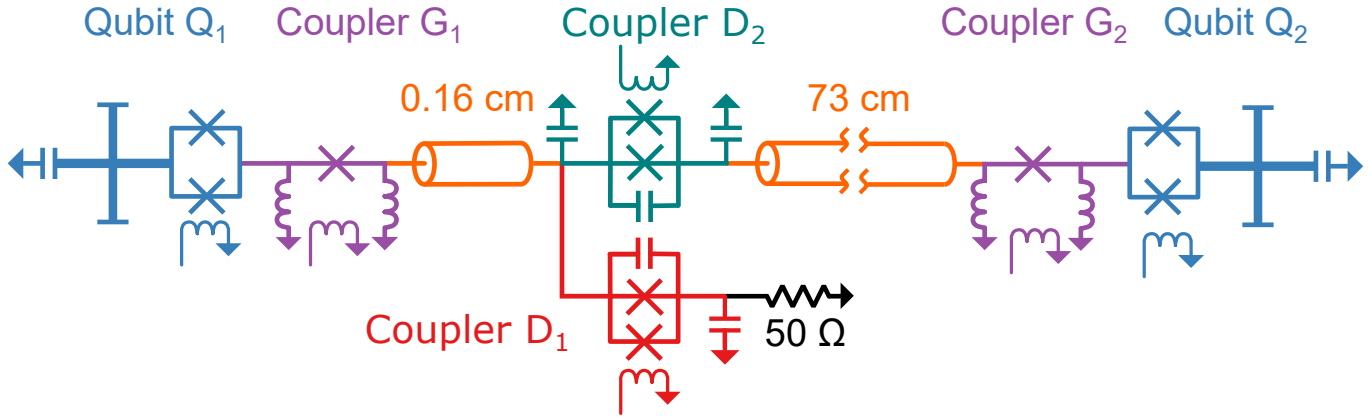


Figure S1. Circuit diagram for the experimental device. The qubits are in blue, their tunable couplers in purple, the two couplers making up the switch in teal and red, the transmission line in orange, and the 50 Ω load in black.

A. Superconducting qubits

The superconducting qubits used in this experiment are frequency-tunable planar transmons [2, 3]. Microwave lines capacitively-coupled to each qubit are used to generate qubit rotations about the X and Y axes of the Bloch sphere; Z -axis rotations and frequency tuning of each qubit are controlled using dc flux-bias lines inductively-coupled to each qubit's two-Josephson junction SQUID loop. To prevent spurious cross-excitations between the two qubits, the qubits are typically de-tuned from one another by 85 MHz, and each qubit's coupler G_1 (G_2) is turned off during qubit state preparation and readout. Each qubit's intrinsic qubit lifetime, coherence time, and idle frequency are provided in Table S2. Each qubit is read out simultaneously with the other qubit, using a dispersive single-shot readout [4, 5] via a capacitively-coupled quarter-wave coplanar waveguide resonator. We used a traveling-wave parametric amplifier [6] (MIT Lincoln Laboratories) to ensure nearly quantum-limited amplification of the readout signals. The $|g\rangle$ and $|e\rangle$ state readout fidelities for each qubit are shown in Table S2.

B. Flux-tunable couplers

The tunable coupling between each qubit and the communication channel is controlled via a galvanically-connected variable coupling π -bridge [1, 7], labeled as G_1 and G_2 in Fig. S1. A dc flux-bias line affords flux control of each coupler by changing its Josephson junction inductance. However, changes in the coupler junction inductance induces a sympathetic frequency shift in

the qubit connected to that coupler, as the inductance of the qubit is modified as well. Similarly, changes in the coupler junction inductance also shifts the transmission line frequency. We calibrate these frequency shifts for all qubit frequencies and coupling strengths used in the adiabatic transfer process. This ensures that the qubits and the channel mode remain in frequency resonance during the transfer, and that the couplings g_1 and g_2 vary precisely according to the desired sine and cosine forms described in the main text. We further note that our choice of total transfer time $t_f = 132$ ns corresponds to control pulses with < 2 MHz bandwidth, far below the maximum bandwidth of our control electronics (250 MHz).

C. Communication channel

The communication channel connecting the two qubits comprises a 0.73 m-long, on-chip coplanar waveguide. To suppress unwanted slotline modes, the transmission line is spanned by air-bridge crossovers every 2 mm, connecting the ground planes on either side of the transmission line [1]. Each resonant standing mode n in the approximately short-circuited line can be modeled as a series RLC resonant circuit with the equivalent lumped-element parameters [8].

$$R_n = Z_0 \alpha \ell, \quad (\text{S1})$$

$$L_n = \frac{1}{2} \mathcal{L} \ell, \quad (\text{S2})$$

$$C_n = \frac{1}{\omega_n^2 L_n}, \quad (\text{S3})$$

where $Z_0 = 50 \Omega$ is the characteristic impedance of the line, determined by geometry and substrate, $\alpha = 0.010$ dB/m is the (lossy) real part of the propagation parameter, determined from the intrinsic resonant mode lifetime $T_{1r,\text{int}}$, $\mathcal{L} = 402$ nH/m is the inductance per unit length, $\ell = 0.73$ m is the total length, and $\omega_n = n\omega_{FSR} = n \times 2\pi \cdot 84$ MHz is the resonant frequency of the n th standing mode.

D. Tunable switch

The tunable switch placed near qubit Q_1 and its tunable coupler G_1 consists of two couplers, D_1 and D_2 , each comprising a DC SQUID in line with each branch of the network. These are used to control the flow of microwave signals through the coupler network. SQUID D_1 connects to an off-chip $50\ \Omega$ load via a wire bond connection, yielding a variable dissipative cold load to the system, while SQUID D_2 connects to the transmission line leading to the tunable coupler G_2 and qubit Q_2 . When the SQUID plasma frequency is close to resonance with an incoming signal, the SQUID presents a high-impedance load that almost completely reflects the signal, while when the SQUID frequency is tuned well away from the signal frequency, nearly unit transmission is achieved. Independent experiments on identically-designed SQUID circuits were used to measure signal transmission through the SQUID as a function of tuning flux, and demonstrate greater than 1 GHz bandwidth with on/off ratios in excess of 35 dB [9]. The transmission dependence on bias flux as well as its frequency dependence for a typical SQUID are shown in Fig. S2.

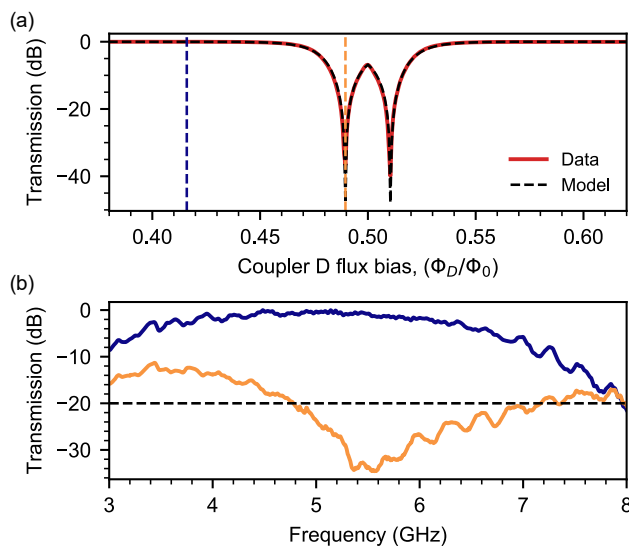


Figure S2. Characterization of a DC SQUID tunable switch, designed identically to those used in the experiments in the main text. (a) Transmission through the SQUID tunable switch as a function of flux bias. The on and off flux settings are marked by blue and orange dashed vertical lines. Dashed lines are results from a circuit model. (b) Transmission measured as a function of frequency near 5.5 GHz for the on (blue) and off (orange) SQUID settings. These demonstrate an on/off ratio greater than 35 dB, isolation bandwidth (below -20 dB) of about 2.9 GHz, and transmission bandwidth (above -1 dB) larger than 1 GHz. The dashed line is the -20 dB transmission threshold used to define the isolation bandwidth.

II. QUANTUM STATE AND PROCESS TOMOGRAPHY

A. Readout correction

The qubit readout fidelities are displayed in Table S2. These are measured by preparing each qubit in $|g\rangle$ or $|e\rangle$ and performing measurements in the two-qubit basis, $|gg\rangle$, $|ge\rangle$, $|eg\rangle$ and $|ee\rangle$. These yield an assignment probability matrix, which is used for readout error correction through linear inversion [10, 11]. A typical assignment probability matrix is shown in Eq. S4. In the

main text, we display the qubit excited state populations, and the quantum process and state tomography fidelities, which are all corrected for measurement errors. As shown in Table S1, there is a modest difference between fidelities obtained with or without these readout corrections.

$$M = \begin{bmatrix} 0.926 & 0.107 & 0.114 & 0.013 \\ 0.040 & 0.865 & 0.005 & 0.120 \\ 0.033 & 0.005 & 0.853 & 0.107 \\ 0.001 & 0.023 & 0.028 & 0.759 \end{bmatrix} \quad (\text{S4})$$

B. Quantum state tomography

We carry out quantum state tomography by applying the single tomography gates $\{I, R_x^{\pi/2}, R_y^{\pi/2}\}$ and then reading out both qubits simultaneously. The density matrix is reconstructed using linear inversion to correct for measurement error and validated to ensure the resulting density matrix ρ is Hermitian, positive, and semi-definite with unit trace [10, 12]. In the experiment, Q_2 's tomography pulse is rotated by a calibrated azimuthal angle φ on the Bloch sphere to account for the phase accumulated from the relative detunings of the two qubits during the transfer sequence.

C. Quantum process tomography

We perform quantum process tomography by preparing four representative single-qubit input states at the sending qubit, $\{|g\rangle, (|g\rangle + |e\rangle)/\sqrt{2}, (|g\rangle + i|e\rangle)/\sqrt{2}, |e\rangle\}$, and subsequently carrying out the state transfer protocol. At the end of the transfer, we measure the resulting density matrix for the receiver qubit via quantum state tomography, and we calculate the process fidelity through linear inversion. The process matrix is validated to ensure that it is positive, Hermitian, and semi-definite with unit trace [13]. In Table S1, we show the process fidelities and trace distances obtained using the adiabatic protocol for the six dissipation settings explored in the main text.

T_{1r} (ns)	Fidelity \mathcal{F}_m	Fidelity (corrected) \mathcal{F}_c	Trace distance \mathcal{D}
28.7 ± 0.2	0.77 ± 0.01	0.79 ± 0.01	0.05
49.8 ± 0.3	0.80 ± 0.01	0.83 ± 0.01	0.06
101.1 ± 0.7	0.86 ± 0.01	0.87 ± 0.01	0.03
336 ± 3	0.91 ± 0.01	0.92 ± 0.01	0.03
503 ± 5	0.92 ± 0.01	0.93 ± 0.01	0.02
3410 ± 40	0.93 ± 0.01	0.96 ± 0.01	0.02

Table S1. Quantum process tomography for adiabatic state transfer at each dissipation level in the channel described in the main text. The measured fidelity is calculated from $\mathcal{F}_m = \text{Tr}(\chi_m \cdot \chi_{\text{ideal}})$, where χ_m is the process matrix without measurement correction, and the measurement-corrected fidelity $\mathcal{F}_c = \text{Tr}(\chi_c \cdot \chi_{\text{ideal}})$, where χ_c is corrected for readout error. The trace distance is calculated from $\mathcal{D} = \sqrt{\text{Tr}([\chi_c - \chi_{\text{sim}}]^2)}$.

III. THEORY OF ADIABATIC STATE TRANSFER

A. State transfer via the dark state

We present here the theory for the adiabatic protocol implemented in the experiments described in the main text. We assume the three quantum systems (qubit Q_1 , the transmission line standing mode, and qubit Q_2), are all frequency-resonant, and we restrict the discussion to the single-excitation subspace of this system. We can write the relevant terms in the system Hamiltonian in the rotating frame of the coupled system as

$$H/\hbar = g_1(t)(|e0g\rangle\langle g1g| + |g1g\rangle\langle e0g|) + g_2(t)(|g0e\rangle\langle g1g| + |g1g\rangle\langle g0e|), \quad (\text{S5})$$

where $g_1(t)$ is the time-dependent coupling between qubit Q_1 and the transmission line standing mode, and $g_2(t)$ that for qubit Q_2 .

Diagonalizing the Hamiltonian reveals three instantaneous eigenstates of the coupled system:

$$|B_{\pm}(t)\rangle = \frac{1}{\sqrt{2}} (\sin \theta(t)|e0g\rangle + \cos \theta(t)|g0e\rangle \pm |g1g\rangle), \quad (\text{S6})$$

$$|D(t)\rangle = \cos \theta(t)|e0g\rangle - \sin \theta(t)|g0e\rangle, \quad (\text{S7})$$

where the instantaneous mixing angle $\theta(t)$ is given by

$$\tan \theta(t) = g_1(t)/g_2(t). \quad (\text{S8})$$

The “dark” eigenstate $|D(t)\rangle$ has no occupancy in the transmission line mode and is at zero energy. The two eigenstates $|B_{\pm}(t)\rangle$ are the so-called “bright” states, as they include photon occupancy of the transmission line mode. These states have the eigenenergies $E_{\pm} = \pm\hbar\bar{g}$ respectively, where $\bar{g} = \sqrt{g_1(t)^2 + g_2(t)^2}$.

The dressed eigenstates can be revealed using qubit spectroscopy. In Fig. S3, with Q_2 resonant with the channel mode and with fixed couplings $g_1 = g_2$, sweeping Q_1 's frequency through the channel mode frequency reveals three eigenstates separated in frequency by $g_{1,2}/2\pi$, as expected. A numerical simulation (Fig. S3b) correctly identifies the middle eigenstate as the dark state $|D(t)\rangle$, with no occupancy in the channel, with the other two eigenstates above and below $|D(t)\rangle$ identified as the two bright states $|B_{\pm}(t)\rangle$.

The adiabatic protocol uses the dark state $|D(t)\rangle$ to achieve the desired state transfer from Q_1 to Q_2 without populating the channel mode. This is achieved by using the sine and cosine time dependence for g_1 and g_2 respectively, as described in the main text, such that the dark state is $|e0g\rangle$ at $t = 0$ and $|g0e\rangle$ at $t = t_f$, and varies smoothly between these limits during the transfer.

B. Adiabatic condition

As the adiabatic protocol relies on remaining in the dark eigenstate throughout the transfer, the protocol needs to be executed slowly, to minimize non-adiabatic errors from coupling to the bright eigenstates. We control for this here by ensuring that integral of the two coupling functions in time satisfies [14–19]

$$\int_0^{t_f} \bar{g}(t) dt = \int_0^{t_f} \sqrt{g_1^2 + g_2^2} dt \approx 4\pi, \quad (\text{S9})$$

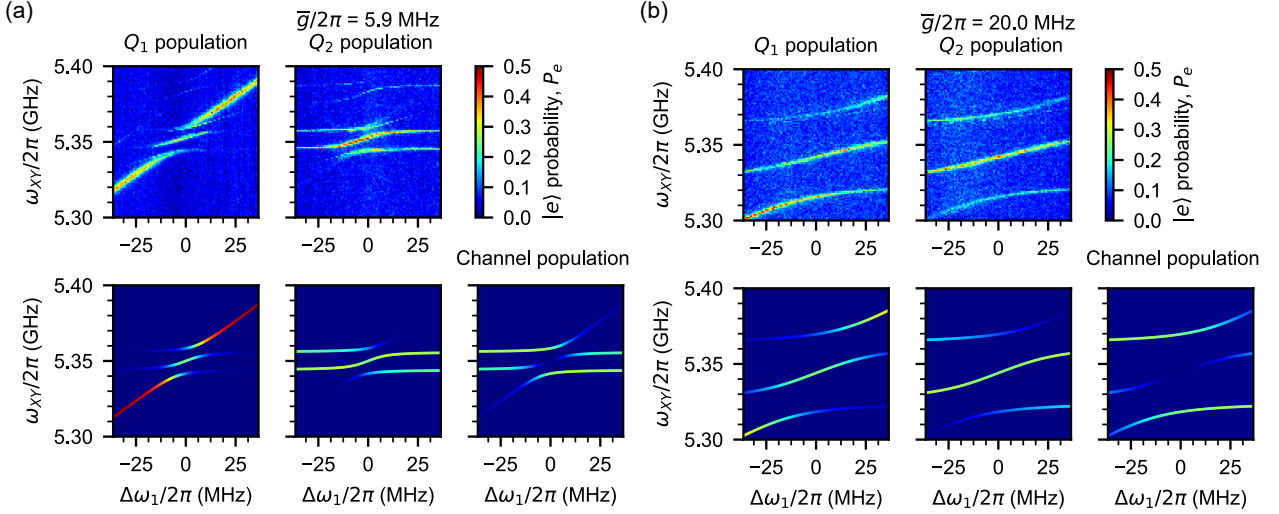


Figure S3. Two-qubit coupled spectroscopy near the resonant channel mode $\omega_r/2\pi = 5.351$ GHz at two coupler settings, (a) $g_1/2\pi = g_2/2\pi = 5.9 \pm 0.1$ MHz and (b) $g_1/2\pi = g_2/2\pi = 20.0 \pm 0.1$ MHz. Upper panels are experimental measurements, lower panels are numerical simulations. Q_2 is set to be resonant with the channel mode and Q_1 is biased to frequency $\omega_r + \Delta\omega_1$, where $\Delta\omega_1$ is varied along the horizontal axis. Qubit spectroscopy is carried out by driving Q_1 with a weak 5 μ s-long pulse at each frequency $\omega_{XY}/2\pi$, then simultaneously measuring each qubit's excited state population P_{e,Q_1} and P_{e,Q_2} using dispersive readout [4, 5]. The two bright states are frequency-offset from the zero-energy dark eigenstate by the coupling $\pm\bar{g}/2\pi = \pm\sqrt{g_1^2 + g_2^2}/2\pi$.

which is much greater than the usual minimum threshold of $3\pi/2$ for efficient state transfer with greater than 85% efficiency [14].

We note that the simple coupling scheme adopted here keeps the effective coupling $\bar{g} = \sqrt{g_1^2 + g_2^2}$ constant, and correspondingly the energy splittings between the eigenstates are constant during the transfer. This type of coupling scheme is known as a parallel adiabatic passage (PAP) and is commonly adopted in STIRAP-like adiabatic protocol, as non-adiabatic errors are minimized by avoiding anti-level crossing points during the transfer [19, 20].

IV. MASTER EQUATION MODEL

We model the quantum behavior of the coupled system using the multi-mode Jaynes-Cummings Hamiltonian H . Our simulation model comprises two qubits (lowering operators σ_1, σ_2) coupled to $2N + 1$ harmonic oscillator modes (lowering operators a_n). We can write the coupled Hamiltonian in the rotating frame of the resonant channel mode as

$$H/\hbar = \Delta\omega_1\sigma_1^\dagger\sigma_1 + \Delta\omega_2\sigma_2^\dagger\sigma_2 + \sum_{n=-N}^N \Delta_n a_n^\dagger a_n \quad (\text{S10})$$

$$+ \sum_{n=-N}^N g_1(t) (\sigma_1 a_n^\dagger + \sigma_1^\dagger a_n) + \sum_{n=-N}^N g_2(t) (-1)^n (\sigma_2 a_n^\dagger + \sigma_2^\dagger a_n), \quad (\text{S11})$$

where $\Delta\omega_{1,2}$ are the qubit detunings from the central resonant mode $n = 0$, $\Delta_n = n\omega_{\text{FSR}}$ is the detuning of the n th channel mode from the $n = 0$ central mode, and $g_1(t)$ and $g_2(t)$ are the time-dependent couplings of Q_1 and Q_2 to the n th channel mode, assumed to be independent of n . This is justified by the high mode number (~ 64) of the resonant channel modes used;

neighboring modes thus have similar coupling strength. We further note that even and odd channel modes have different signs for g_2 compared to g_1 , owing to the parity of their wavefunctions $\psi_n(x)$ [21, 22].

To simulate the time-domain evolution of our coupled quantum system, we numerically integrate the Lindblad master equation[23, 24] with the Hamiltonian using the python package QuTiP [25]. We account for qubit relaxation and decoherence by including the Lindblad collapse operators $\sigma_-/\sqrt{T_{1,\text{int}}}$ and $\sigma_z/\sqrt{2T_\phi}$, where $1/T_\phi = 1/T_{2,\text{Ramsey}} - 1/2T_{1,\text{int}}$. The energy lifetime of the channel modes T_{1r} is taken to be identical for all oscillator modes and is accounted for by the Lindblad collapse operators $a_n/\sqrt{T_{1r}}$. Qubit parameters are obtained from independent qubit measurements, while T_{1r} is obtained using the method outlined in Fig. 2 of the main text. The numerical simulations include $2N + 1 = 5$ modes, each containing two Fock states $|0\rangle$ and $|1\rangle$. The coupling functions $g_{1,2}(t)$ are varied dynamically in time using the coupling described in Fig. 3 of the main text. We use this model to simulate the time evolution of Q_1 and Q_2 in Fig. 3 of the main text as well as to obtain the expected process and Bell state fidelities, which account for the finite qubit lifetime and coherence (Fig. 3, 4).

V. ADIABATIC PROTOCOL IN THE STRONG MULTI-MODE COUPLING REGIME

Using the master equation model (see above), we explore the performance of our adiabatic protocol as it approaches the strong multi-mode coupling regime, where the coupling between the qubit and the channel mode is of order the free spectral range ($\bar{g} \sim \omega_{FSR}$). We quantify the performance of the protocol by calculating the maximum transfer efficiency η attainable at each effective coupling \bar{g} . The results of the simulations are shown in Fig S4. This simulation includes $2N + 1 = 15$ channel modes, each containing two Fock states $|0\rangle$ and $|1\rangle$. We did not perform numerical simulations for $\bar{g}/\omega_{FSR} > 1$, as this requires including more than 17 channel modes in the coupled Hamiltonian in Eq. (S10) for accurate simulations, consuming significant computational resources for the resultingly large Hilbert space.

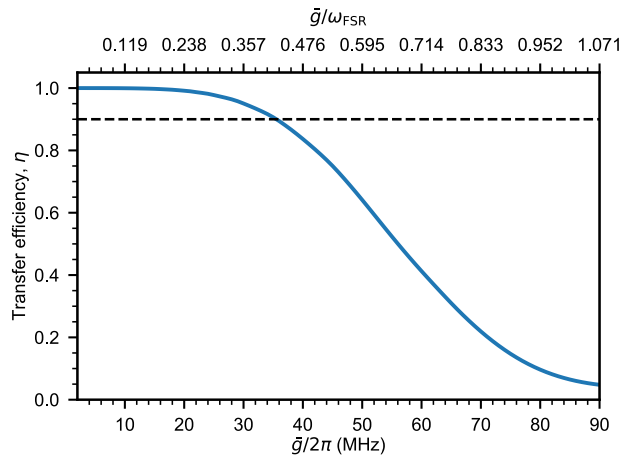


Figure S4. Calculated maximum transfer efficiency η as a function of the coupling strength \bar{g} . In the numerical simulation, the free spectral range of the channel is kept fixed at $\omega_{FSR}/2\pi = 84$ MHz, while the effective coupling strength \bar{g} is varied. For coupling strengths $\bar{g}/2\pi \gtrsim 36$ MHz, interference effects from interactions with neighboring resonant modes become significant, reducing the transfer efficiency attainable with the adiabatic protocol. Dashed line marks where $\eta = 90\%$.

VI. SPURIOUS COUPLING OF Q_1 TO THE EXTERNAL LOAD

The primary source of infidelity for the adiabatic protocol is the reduced lifetime of Q_1 when the couplers G_1 and D_1 are both turned on, as this couples both the channel mode and the qubit to the external 50Ω load. In the ideal case, this coupler only changes the loss in the channel; however, due to the close proximity of Q_1 to this coupler in the circuit, the qubit is also coupled to the 50Ω load. This can be understood by the simplified circuit model shown in Fig. S5a: When Q_1 is exactly resonant with the channel mode, the series resonance presented by the channel (represented by the series $L_r - C_r$ in the diagram) shorts the parallel load resistance $R_{L,\text{eff}}$, so there is little to no effect on the qubit. Conversely, a slight detuning of the qubit from this resonant frequency increases the $L_r - C_r$ impedance, so the external load is no longer exactly shorted and can load the qubit. This substantially reduces Q_1 's T_1 lifetime when the coupler to the load is turned on. We model this effect by first calculating the effective external load $R_{L,\text{eff}}$ at each dissipation settings in the channel mode

$$\frac{1}{T_{1r,\text{ext}}} = \frac{1}{T_{1r}} - \frac{1}{T_{1r,\text{int}}} \quad (\text{S12})$$

$$R_{L,\text{eff}} = \frac{L_r}{T_{1r,\text{ext}}} \quad (\text{S13})$$

Next, we calculate the equivalent impedance $Z(\Delta\omega_1)$ as seen by the qubit as a function of detuning from the channel mode (Fig. S5b). The loaded qubit lifetime T_1 is then given by:

$$T_1 = L_q / \text{Re}[Z(\Delta\omega_1)] \quad (\text{S14})$$

In Fig. S5c,d, we show the calculated energy relaxation time T_1 of Q_1 due parasitic coupling to the external load at the largest loss case explored here ($T_{1r} = 28.7$ ns) using circuit parameters listed in Table S2. In Fig. S5c, we see that for the coupling $|g_1|/2\pi = 15$ MHz, a 0.4 MHz frequency detuning can reduce Q_1 's T_1 to 500 ns. We further show the coupling strength dependence of this effect assuming a constant detuning in Fig. S5d. The relaxation of Q_1 for each dissipation setting due to this parasitic coupling has been included in the simulation

A possible way to overcome this non-ideality and increase the transfer efficiency of the adiabatic protocol further is to decrease the total transfer time t_f , reducing the impact of loss from Q_1 . However, this comes at the cost of populating the channel mode during the transfer, as a result of the reduced adiabaticity. We explore these trade-offs for the largest dissipation case explored here using the master equation model with actual device parameters outlined in Table S2. In Fig. S6, we show that a maximum transfer efficiency of $\eta = 0.73$ is possible with a $t_f = 66$ ns, 0.06 higher than the efficiency achieved in the experiment in the largest loss case, where $T_{1r} = 28.7$ ns, with a total transfer time of $t_f = 132$ ns. We also note that in Fig. S6, our choice of $t_f = 132$ ns in the experiment is a local maximum; this is not coincidental and is expected from theory. The time corresponds to the periodic return of the dark state at discrete times $t_f = (2\pi/\bar{g})\sqrt{n^2 - (1/4)^2}$ for non-zero integer n [26]. For $\bar{g}/2\pi = 15$ MHz, our choice of total transfer time $t_f = 132$ ns is the $n = 2$ case.

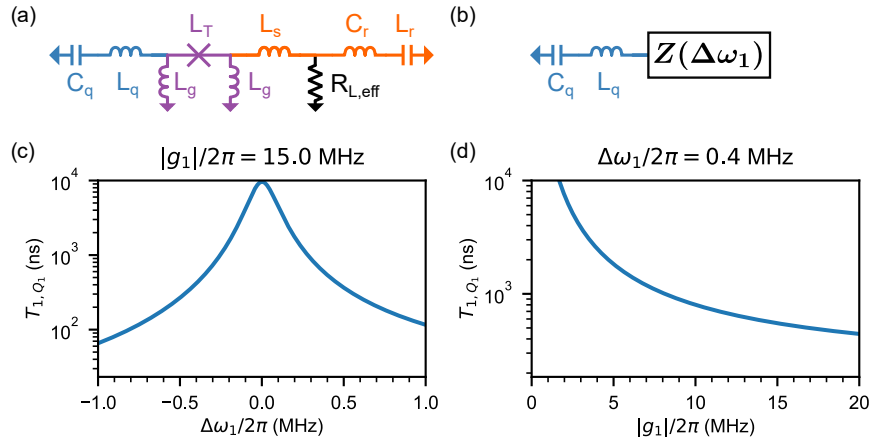


Figure S5. (a) Electrical circuit for calculating the parasitic loading of Q_1 from the external $50\ \Omega$ load. The qubit is represented by the series $C_q - L_q$; the coupler by the π bridge circuit $L_g - L_T - L_g$; the short length of transmission line to the load $R_{L,eff}$ by L_s ; and finally the lumped model for the channel resonant mode is represented by the series $L_r - C_r$. We then transform the right-half of the circuit to an equivalent impedance $Z(\Delta\omega_1)$ as seen by the qubit (b). We use this circuit model to calculate the loaded energy relaxation times of Q_1 as a function of both detuning from the channel mode $\Delta\omega_1$ and coupling $|g_1|$ using circuit parameters listed in Table S2. (c) Calculated Q_1 relaxation times as a function of detunings from the resonant mode for the largest dissipation case ($T_{1r} = 28.7$ ns) and with coupling $|g_1|/2\pi = 15$ MHz. (d) Calculated Q_1 relaxation times as a function of coupling $|g_1|$ assuming a constant detuning of 0.4 MHz from the resonant mode.

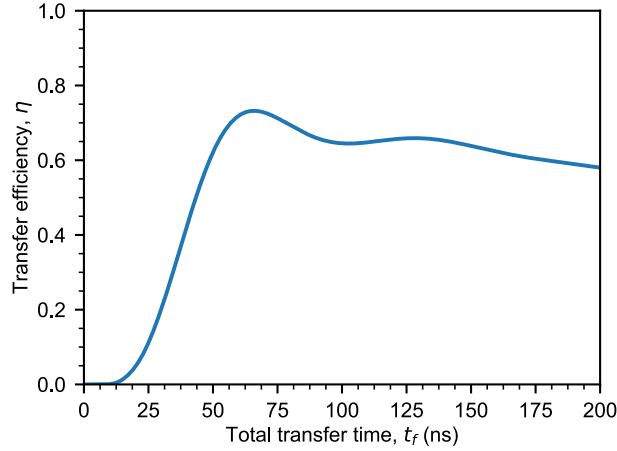


Figure S6. Calculated maximum transfer efficiency as a function of transfer time t_f for the largest loss case explored in the experiment, where $T_{1r} = 28.7$ ns. A maximum transfer efficiency of 0.73 occurs at transfer time of $t_f = 66$ ns, 0.06 higher than the efficiency achieved in the experiment with $t_f = 132$ ns.

VII. CONCURRENCE

The two-qubit concurrence \mathcal{C} of the Bell singlet state is calculated from the reconstructed density matrix ρ using the standard definition [27, 28]:

$$\mathcal{C}(\rho) \equiv \max\{0, \lambda_1 - \lambda_2 - \lambda_3 - \lambda_4\} \quad (\text{S15})$$

where λ_i are the square roots of the eigenvalues of the matrix $\rho(\sigma_y \otimes \sigma_y)\rho^*(\sigma_y \otimes \sigma_y)$, in descending order and ρ^* is the elementwise complex conjugate of the density matrix ρ .

VIII. ADDITIONAL QUANTUM STATE TRANSFER AND REMOTE ENTANGLEMENT MEASUREMENTS

In Fig. S7–S10, we show additional measurements similar to those shown in Fig. 3a,b of the main text, for other dissipation settings in the channel mode. These measurements were made using both the adiabatic protocol and the relay method. Results from a master equation simulation, accounting for channel dissipation as well as qubit imperfections are shown as well.

Qubit parameters	Qubit 1	Qubit 2
Qubit maximum frequency, $\omega_{ge}^{max}/2\pi$ (GHz)	6.239	6.132
Qubit idle frequency, $\omega_{ge}^{idle}/2\pi$ (GHz)	5.504	5.419
Qubit capacitance, C_q (design value) (fF)	90	90
Qubit SQUID inductance, L_q (nH)	7.2	7.5
Qubit anharmonicity, $\alpha/2\pi$ (MHz)	-168	-171
Qubit intrinsic lifetime, $T_{1,int}$ (μ s)	11.5(5)	9.1(2)
Qubit Ramsey dephasing time, $T_{2,Ramsey}$ (μ s)	1.11(3)	1.15(3)
Qubit spin-echo dephasing time, T_{2E} (μ s)	4.09(5)	3.54(4)
$ g\rangle$ state readout fidelity, F_g	0.966(3)	0.959(4)
$ e\rangle$ state readout fidelity, F_e	0.881(5)	0.888(8)
Readout resonator frequency, $\omega_r/2\pi$ (GHz)	6.361	6.415
Readout resonator quality factor, Q_r	6.9×10^3	6.4×10^3
Readout dispersive shift, $\chi_r/2\pi$ (MHz)	0.15	0.15

Flux-tunable couplers parameters	Coupler G_1	Coupler G_2
Coupler junction inductance, L_T (nH)	0.61	0.61
Coupler grounding inductance, L_g (design value) (nH)	0.2	0.2

Tunable switch parameters	Coupler D_1	Coupler D_2
Coupler SQUID inductance, L_J (nH)	0.34	0.34
Coupler SQUID capacitance, C_J (fF)	125	125
Coupler grounding capacitance, C_g (design value) (fF)	100	100

Table S2. Device parameters for the two qubits, the flux-tunable couplers connecting each qubit to the channel, and the DC SQUID tunable couplers making up the tunable switch that couple the channel to an external 50Ω load.

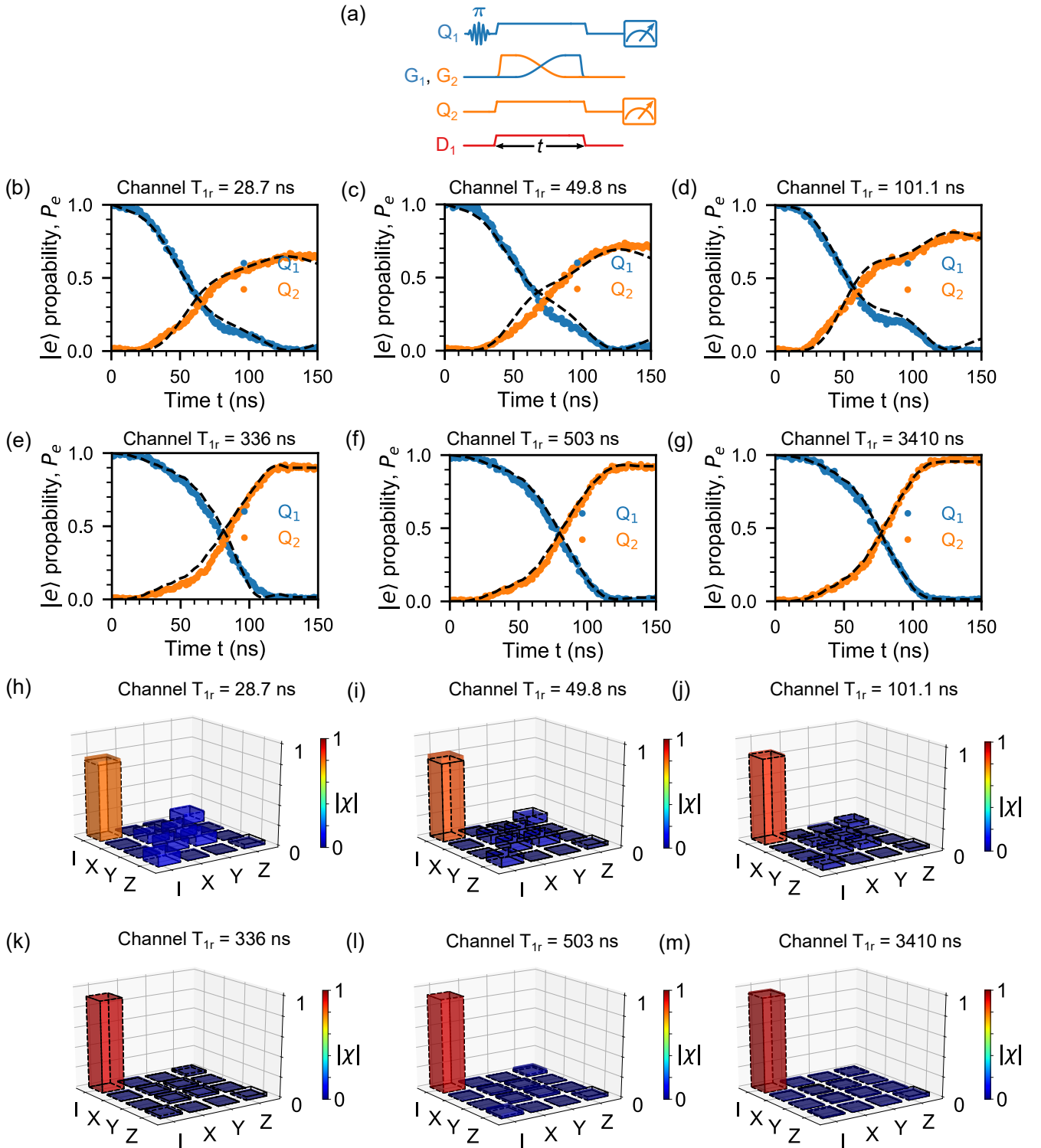


Figure S7. Quantum state transfer using the adiabatic protocol. (a) Control pulse sequence. (b-g) Adiabatic state transfer between qubits Q_1 and Q_2 , measured with different dissipation settings for the resonant channel mode, quantified by the resonant mode lifetime T_{1r} . Blue (orange) circles represent simultaneously measured excited state populations of Q_1 (Q_2) at time t . (h-m) Quantum process tomography at the maximum transfer efficiency point for each dissipation setting in panels b-g. In all panels, dashed lines are the results from master equation simulations, accounting for channel dissipation and qubit imperfections.

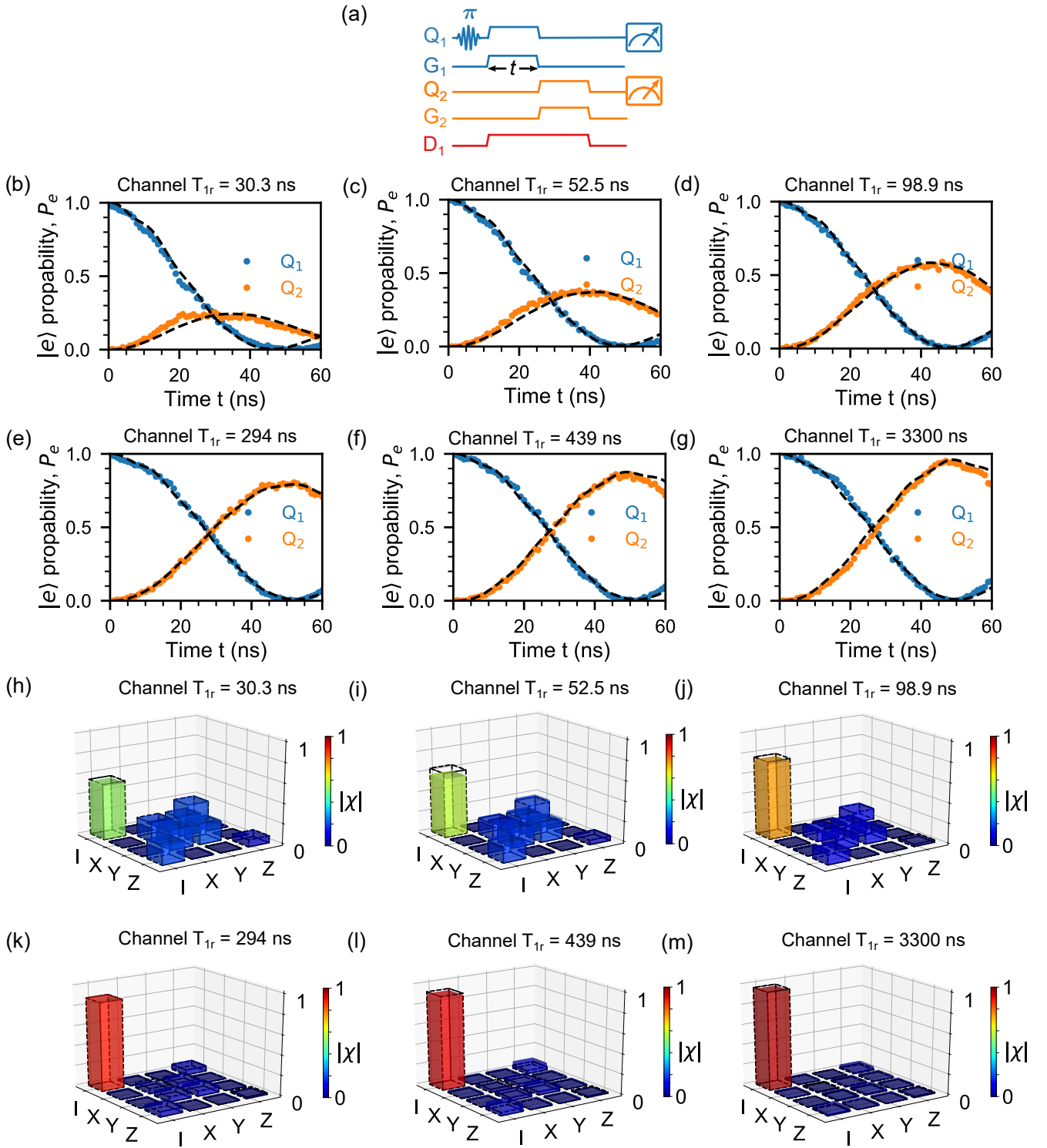


Figure S8. Quantum state transfer using the relay method. (a) Control pulse sequence. (b-g) Quantum state transfer from Q_1 to Q_2 using the resonant channel mode as a relay, measured with different dissipation settings for the resonant channel mode, quantified by the resonant mode lifetime T_{1r} . Blue (orange) circles represent simultaneously measured excited state populations of Q_1 (Q_2) versus swap time t . (h-m) Quantum process tomography at the maximum transfer efficiency point for each dissipation setting in panels b-g. In all panels, dashed lines are the results from master equation simulations, accounting for channel dissipation and qubit imperfections.

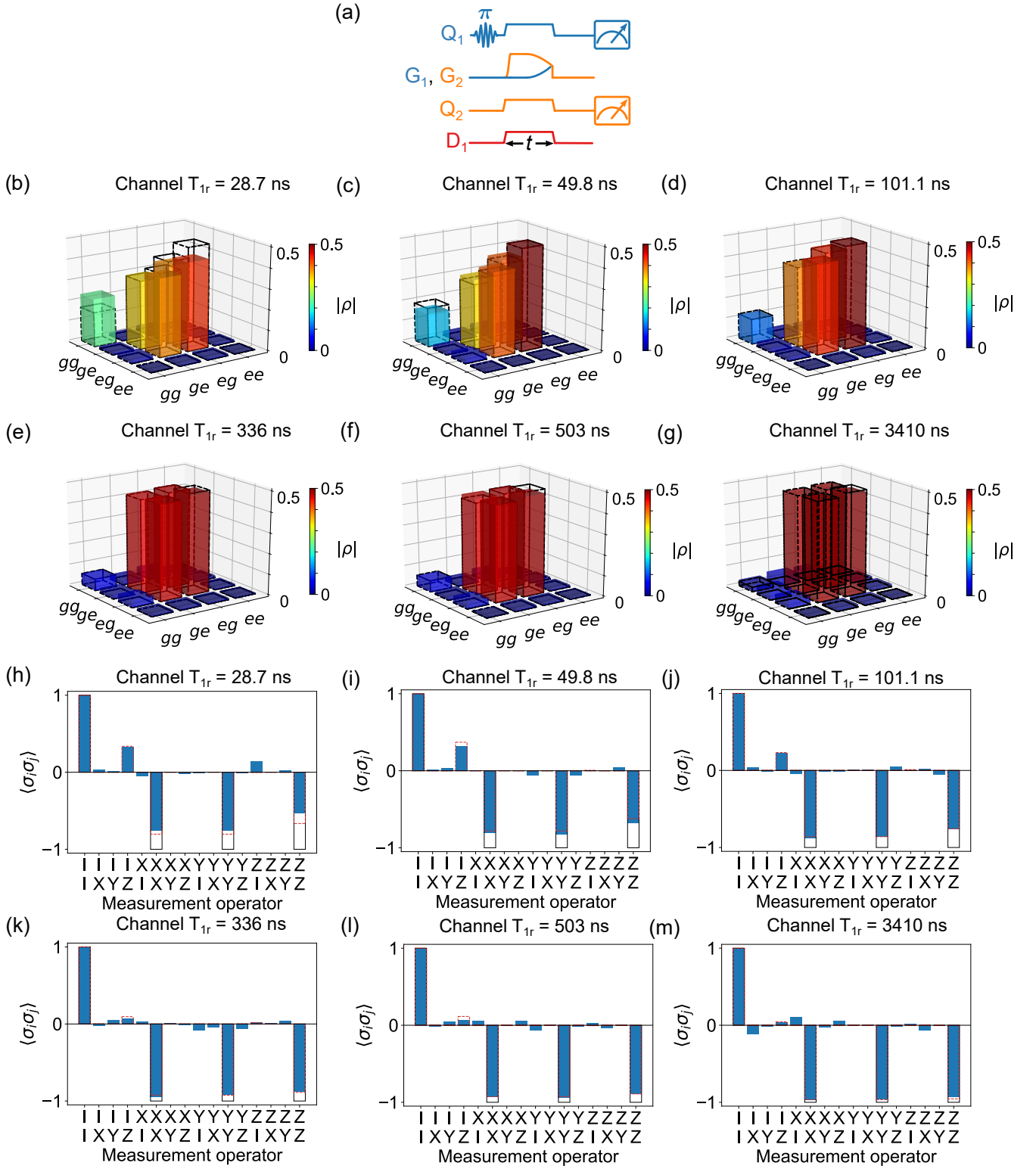


Figure S9. Remote entanglement using the adiabatic protocol. (a) Control pulse sequence. (b-g) Reconstructed density matrix of the Bell states generated using the adiabatic protocol, measured with different dissipation settings for the resonant channel mode, quantified by the resonant mode lifetime T_{1r} . (h-m) Expectation values for the two-qubit Pauli operators $\langle \sigma_i \sigma_j \rangle$ for the Bell state density matrix in panels b-g. Solid lines show the expectation values for the ideal Bell singlet state $|\psi^-\rangle = (|e0g\rangle - |g0e\rangle) / \sqrt{2}$. In all panels, dashed lines are the results from master equation simulations, accounting for channel dissipation and qubit imperfections.

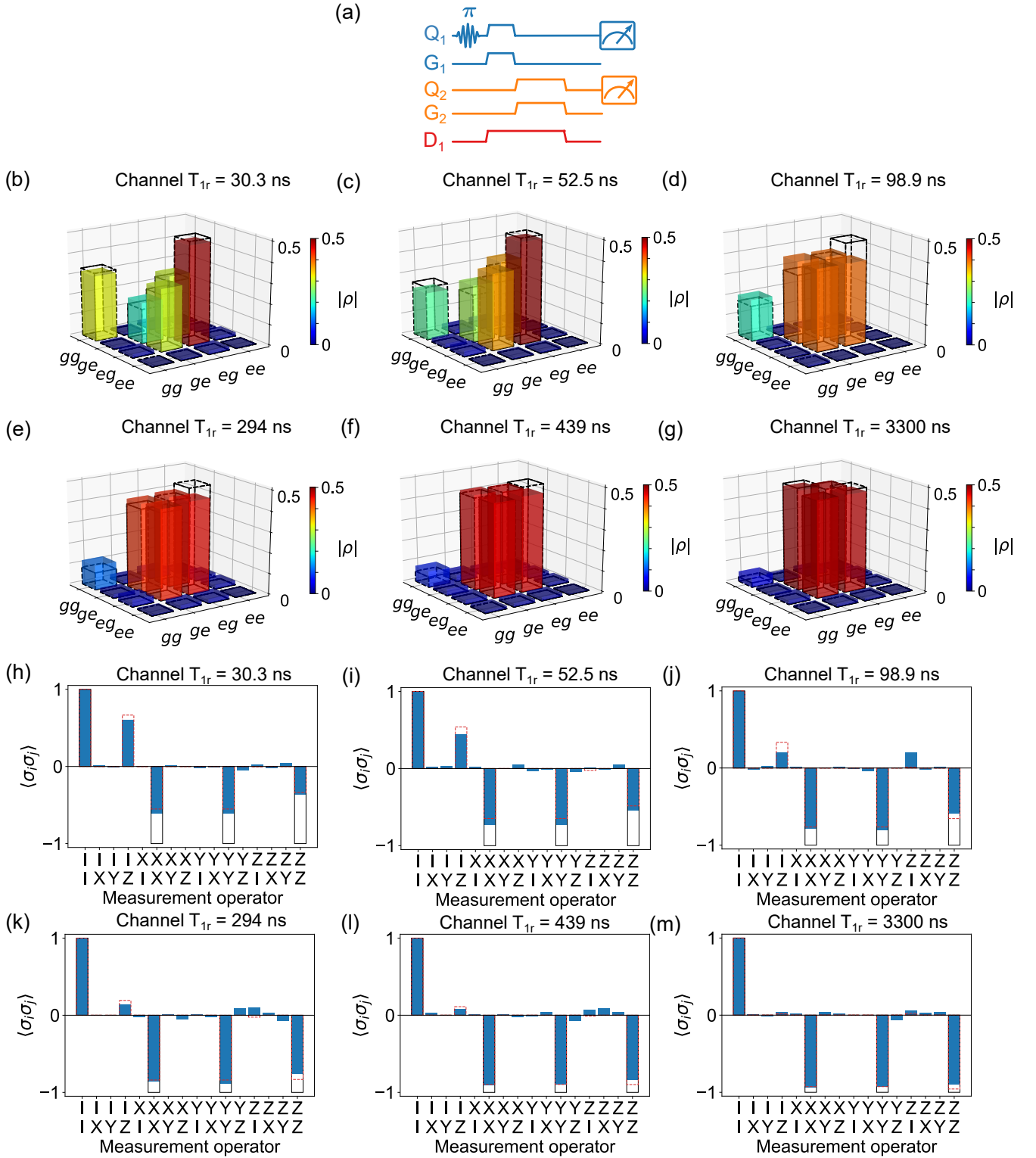


Figure S10. Remote entanglement using the relay method. (a) Control pulse sequence. (b-g) Reconstructed density matrix of the Bell states generated with the relay method, measured with different dissipation settings for the resonant channel mode, quantified by the resonant mode lifetime T_{1r} . (h-m) Expectation values for the two-qubit Pauli operators $\langle \sigma_i \sigma_j \rangle$ for the Bell state density matrix in panels b-g. Solid lines show the expectation values for the ideal Bell singlet state $|\psi^-\rangle = (|e0g\rangle - |g0e\rangle) / \sqrt{2}$. In all panels, dashed lines are the results from master equation simulations, accounting for channel dissipation and qubit imperfections.

-
- [1] Y. P. Zhong, H.-S. Chang, K. J. Satzinger, M.-H. Chou, A. Bienfait, C. R. Conner, É. Dumur, J. Grebel, G. A. Peairs, R. G. Povey, D. I. Schuster, and A. N. Cleland, *Nature Physics* **15**, 741 (2019).
- [2] J. Koch, T. M. Yu, J. Gambetta, A. A. Houck, D. I. Schuster, J. Majer, A. Blais, M. H. Devoret, S. M. Girvin, and R. J. Schoelkopf, *Physical Review A* **76**, 042319 (2007).
- [3] R. Barends, J. Kelly, A. Megrant, D. Sank, E. Jeffrey, Y. Chen, Y. Yin, B. Chiaro, J. Mutus, C. Neill, P. O'Malley, P. Roushan, J. Wenner, T. C. White, A. N. Cleland, and J. M. Martinis, *Physical Review Letters* **111**, 080502 (2013).
- [4] E. Jeffrey, D. Sank, J. Y. Mutus, T. C. White, J. Kelly, R. Barends, Y. Chen, Z. Chen, B. Chiaro, A. Dunsworth, A. Megrant, P. J. J. O'Malley, C. Neill, P. Roushan, A. Vainsencher, J. Wenner, A. N. Cleland, and J. M. Martinis, *Physical Review Letters* **112**, 190504 (2014).
- [5] J. Kelly, R. Barends, A. G. Fowler, A. Megrant, E. Jeffrey, T. C. White, D. Sank, J. Y. Mutus, B. Campbell, Y. Chen, Z. Chen, B. Chiaro, A. Dunsworth, I.-C. Hoi, C. Neill, P. J. J. O'Malley, C. Quintana, P. Roushan, A. Vainsencher, J. Wenner, A. N. Cleland, and J. M. Martinis, *Nature* **519**, 66 (2015).
- [6] C. Macklin, K. O'Brien, D. Hover, M. E. Schwartz, V. Bolkhovskoy, X. Zhang, W. D. Oliver, and I. Siddiqi, *Science* **350**, 307 (2015).
- [7] Y. Chen, C. Neill, P. Roushan, N. Leung, M. Fang, R. Barends, J. Kelly, B. Campbell, Z. Chen, B. Chiaro, A. Dunsworth, E. Jeffrey, A. Megrant, J. Y. Mutus, P. J. J. O'Malley, C. M. Quintana, D. Sank, A. Vainsencher, J. Wenner, T. C. White, M. R. Geller, A. N. Cleland, and J. M. Martinis, *Physical Review Letters* **113**, 220502 (2014).
- [8] D. M. Pozar, *Microwave engineering*, 4th ed. (Wiley, Hoboken, NJ, 2012).
- [9] H.-S. Chang, Y. P. Zhong, K. J. Satzinger, M.-H. Chou, A. Bienfait, C. R. Conner, É. Dumur, J. Grebel, G. A. Peairs, R. G. Povey, and A. N. Cleland, In preparation (2020).
- [10] M. Steffen, M. Ansmann, R. C. Bialczak, N. Katz, E. Lucero, R. McDermott, M. Neeley, E. M. Weig, A. N. Cleland, and J. M. Martinis, *Science* **313**, 1423 (2006).
- [11] J. M. Chow, L. DiCarlo, J. M. Gambetta, A. Nunnenkamp, L. S. Bishop, L. Frunzio, M. H. Devoret, S. M. Girvin, and R. J. Schoelkopf, *Physical Review A* **81**, 062325 (2010).
- [12] M. Neeley, R. C. Bialczak, M. Lenander, E. Lucero, M. Mariantoni, A. D. O'Connell, D. Sank, H. Wang, M. Weides, J. Wenner, Y. Yin, T. Yamamoto, A. N. Cleland, and J. M. Martinis, *Nature* **467**, 570 (2010).
- [13] M. Neeley, M. Ansmann, R. C. Bialczak, M. Hofheinz, N. Katz, E. Lucero, A. O'Connell, H. Wang, A. N. Cleland, and J. M. Martinis, *Nature Physics* **4**, 523 (2008).
- [14] N. V. Vitanov, A. A. Rangelov, B. W. Shore, and K. Bergmann, *Reviews of Modern Physics* **89**, 015006 (2017).
- [15] H. K. Xu, C. Song, W. Y. Liu, G. M. Xue, F. F. Su, H. Deng, Y. Tian, D. N. Zheng, S. Han, Y. P. Zhong, H. Wang, Y.-x. Liu, and S. P. Zhao, *Nature Communications* **7**, 11018 (2016).
- [16] K. Bergmann, H. Theuer, and B. W. Shore, *Reviews of Modern Physics* **70**, 1003 (1998).
- [17] B. W. Shore, *Manipulating quantum structures using laser pulses* (Cambridge University Press, Cambridge, UK ; New York, 2011).
- [18] M. O. Scully and M. S. Zubairy, *Quantum optics* (Cambridge University Press, Cambridge ; New York, 1997).
- [19] G. S. Vasilev, A. Kuhn, and N. V. Vitanov, *Physical Review A* **80**, 013417 (2009).
- [20] S. Guerin, S. Thomas, and H. R. Jauslin, *Physical Review A* **65**, 023409 (2002).
- [21] T. Pellizzari, *Physical Review Letters* **79**, 5242 (1997).
- [22] B. Vogell, B. Vermersch, T. E. Northup, B. P. Lanyon, and C. A. Muschik, *Quantum Science and Technology* **2**, 045003 (2017).
- [23] G. Lindblad, *Communications in Mathematical Physics* **48**, 119 (1976).
- [24] D. F. Walls and G. J. Milburn, *Quantum optics*, 2nd ed. (Springer, Berlin, 2008).
- [25] J. Johansson, P. Nation, and F. Nori, *Computer Physics Communications* **183**, 1760 (2012).

- [26] Y.-D. Wang, R. Zhang, X.-B. Yan, and S. Chesi, *New Journal of Physics* **19**, 093016 (2017).
- [27] W. K. Wootters, *Physical Review Letters* **80**, 2245 (1998).
- [28] M. B. Plenio and S. Virmani, *arXiv:quant-ph/0504163* (2006), *arXiv: quant-ph/0504163*.